Optimizing the Architecture of Lung-Inspired Fuel Cells

J. I. S. Cho[a,b,†], J. Marquis[c,†], P. Trogadas[a,b], T. P. Neville[b], D. J. L. Brett[b], M.-O. Coppens*[a]

[a.] *EPSRC "Frontier Engineering" Centre for Nature Inspired Engineering & Department of Chemical Engineering, University College London, London WC1E 7JE, UK*

[b.] *Electrochemical Innovation Lab, Department of Chemical Engineering, University College London, London WC1E 7JE, UK*

[c.] *Department of Chemical and Biological Engineering, Rensselaer Polytechnic Institute, Troy, NY 12180, USA [current address: Momentive Performance Materials, Waterford, NY 12188, USA]*

† Both authors contributed equally

* Corresponding author: Tel.: +44 (0)20 3108 1126 / 7679 3824; Fax: +44 (0)20 7679 7369.
E-mail address: m.coppens@ucl.ac.uk

ABSTRACT

A finite-element model of a polymer electrolyte membrane fuel cell (PEMFC) with fractal branching, lung-inspired flow-field is presented. The effect of the number of branching generations N on the thickness of the gas diffusion layer (GDL) and fuel cell performance is determined. Introduction of a fractal flow-field to homogenize reactant concentration at the flow-field | GDL interface allows for the use of thinner GDLs. The model is coupled with an optimized cathode catalyst layer microstructure with respect to platinum utilization and power density, revealing that the 2020 DoE target of ~ 8 kW/g_{Pt} is met at N = 4 generations, and a platinum utilization of ~ 36 kW/g_{Pt} is achieved at N = 6 generations. In terms of the overall fuel cell stack architecture, our results indicate that either the platinum loading or the number of cells in the stack can be reduced by ~ 75%, the latter option of which, when combined with a 100 μm GDL, can lead to > 80% increase in the volumetric power density of the fuel cell stack.

Keywords: Lung-Inspired; Fractal; Flow-Field; Gas Diffusion Layer; Pt Utilization

1. Introduction

As global energy demands continue to rise, the need for viable alternative energy technologies is at an all-time high. Fuel cells have been amongst the most promising candidates for supplying reliable, clean, and efficient energy for a variety of applications, ranging from personal electronics to cars, homes, and larger commercial power generation. Decades of research have led to design improvements that leave fuel cell technology on the cusp of economic viability [1].

Despite the major advancements made over several decades to improve fuel cell performance and reliability, nearly all polymer electrolyte membrane fuel cell (PEMFC) designs suffer from the same fundamental flaw – depletion of reactant concentration along the flow path of the flow-field [2-5]. Within the confines of traditional flow-field geometries, such as serpentine and parallel, this is an unavoidable side effect. Uneven gas distribution in the flow-fields leads to fuel starvation, which is one of the main causes of component and performance degradation of a fuel cell [6-13]. Efforts to mitigate mass transport losses have led to the development of various flow-field designs [2, 3, 14-19].

Recently, we proposed a nature-inspired engineering methodology that addresses the uneven reactant distribution issues in fuel cells (Fig. 1) [20]. This is the first fuel cell design approach of its kind that is rooted in the mechanistic understanding of the structure of the respiratory organ. The characteristics of the lung to transition from fractal branching, bronchial airways to uniformly distributed acinar airways, corresponding to a transition from convective to diffusive transport (Péclet number, Pé ~ 1) and deliver oxygen uniformly over its entire structure to achieve minimal global entropy production [10, 21, 22], served as a guide towards the design of fractal flow-fields. This nature-inspired engineering approach stands in firm contrast to heuristic approaches that imitate biological features, by copying the apparent structure of

natural fluid distribution systems (*e.g.,* lungs, leaves, and veins) without formal mathematical description or methodology to guide the design of such flow-fields [2, 17, 23-28]. The lung-inspired flow-field design differentiates itself from conventional design approaches, which involve empirical alteration of the channel configurations to achieve more uniform gas distribution, but typically result in a higher pressure drop [29-31] and ineffective water and heat management [29, 30]. Numerical simulations of the lung-inspired flow-field based PEMFCs revealed that the ideal number of branching generations (N) for minimum entropy production lies between N = 5 and 7. Guided by the simulation results, three flow-fields with N = 3, 4, and 5 were 3D printed *via* direct metal laser sintering (DMLS) and tested against serpentine flow-fields. The N = 4 fractal flow-field demonstrated, respectively, ~ 20% and ~ 30% increase in current density and maximum power density over serpentine flow-fields above 0.8 A cm^{-2} [20].

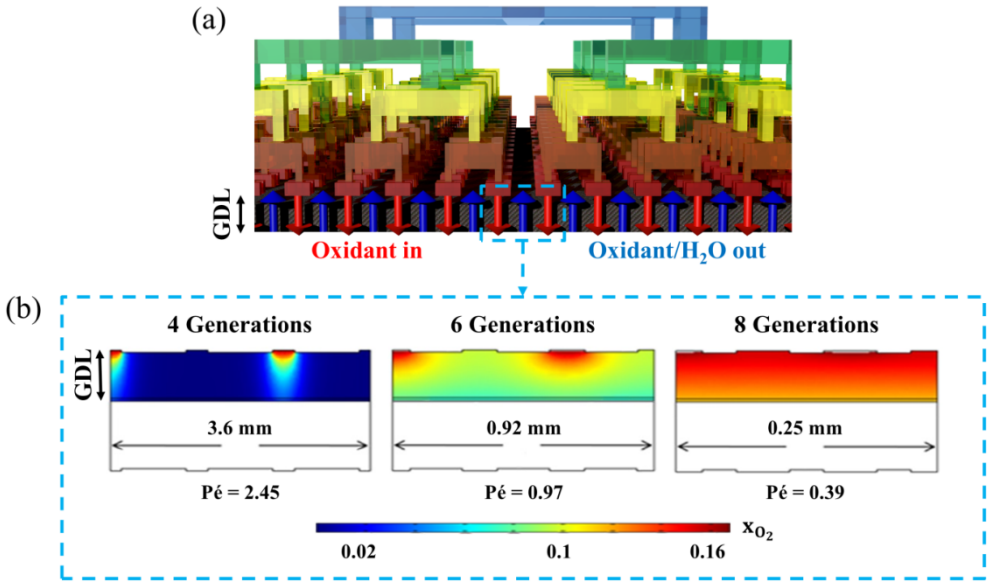

Fig. 1. (a) A computer generated image of the GDL integrated with a fractal flow-field with N = 4 generations, and (b) numerical simulations conducted in our previous study illustrating oxygen mass fraction distribution in the cathode catalyst layer using fractal flow-fields with N = 4, 6, and 8 generations [20]. Copyright © 2018 The Royal Society of Chemistry.

To further improve the fuel cell performance realized from uniform reactant distribution, the electrode structure and composition can be tailored. The electrode of a fuel cell consists of two

77 main components, namely the gas diffusion layer (GDL) and the catalyst layer (CL). The GDL
78 is typically a carbon fiber sheet treated with polytetrafluoroethylene (PTFE) that provides
79 structural support for the membrane electrode assembly (MEA), while allowing gas and
80 electrical transport to and from the catalyst layer [32]. Although the GDL is a seemingly minor
81 component of a fuel cell, studies report that altering its structural properties (such as porosity,
82 PTFE content, and thickness) can substantially affect fuel cell performance [32-34]. Additional
83 gain in performance can be achieved *via* modification of the CL microstructure to improve
84 catalyst utilization at reduced loading [35].
85 Several models have been developed to explore the optimum composition and structure of the
86 cathode catalyst layer in a PEMFC. These can be categorized as interface [36, 37], pseudo-
87 homogeneous [38-42], and agglomerate models [43-50]. Agglomerate models are usually
88 employed due to the better representation of the cathode catalyst layer than the other models,
89 resulting in good agreement with experimental data [39, 51]. This work introduces a finite-
90 element model of a lung-inspired flow-field based PEMFC, and examines the effect of the
91 number of generations N on the thickness of the GDL and the fuel cell performance. Lung-
92 inspired flow-fields perform some of the tasks of the GDL, such as homogenizing reactant
93 concentration, and reducing flow velocity prior to entering the catalyst layer. As a result,
94 thinner GDLs can be used, allowing for a higher concentration of oxygen to reach the catalyst
95 layer. To investigate the effect of the number of generations N on platinum utilization, a finite-
96 element model is combined with a two-phase agglomerate model [35] with optimized cathode
97 catalyst layer microstructure.
98
99
100
101

2. Mathematical model of the flow-field

2.1. Modeling domain

The modeling domain consists of the GDL and CL at the anode and cathode, as well as the polymer electrolyte membrane (Fig. 2). The MEA is located in between fractal flow-fields with a surface area of 10 cm^2, which are represented by arrows that correspond to the location of the fractal inlet and outlet channels.

The model captures the effects of varying the number of branching generations *N* on fuel cell performance by "zooming in" on the flow-field outlets, such that the number of inlets and outlets being modeled remains the same for any given number of generations. However, the size of the modeling domain, along with the size of the inlets, outlets, and land area, changes with each additional generation (Fig. 2). The thickness of the GDL, CL, and polymer electrolyte membrane remains constant, regardless of the number of generations being modeled. Due to the symmetry associated with the fractal design, the results from the modeled section can be extrapolated to locally resolve fuel cell performance throughout the entire cell.

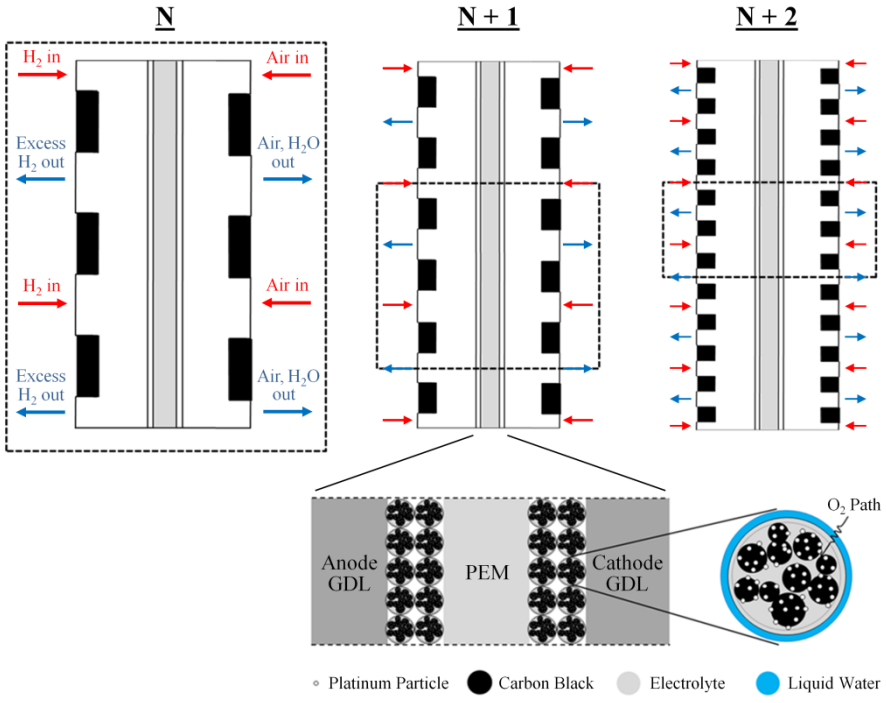

Fig. 2. Schematic of the modeling domain of the lung-inspired flow-field based PEMFC at various generations *N*. The rectangular box shows what is actually being modeled [20].

2.2. Modeling assumptions

The main modeling assumptions are as follows [52, 53]:

Table 1. Assumptions used in the model

- Steady state
- Isothermal operation
- Ideal gases
- Fully humidified inlet gases
- Fully hydrated polymer electrolyte membrane (Nafion)
- Uniform catalyst nanoparticle size and uniform Nafion film thickness on these nanoparticles
- No gas crossover
- Liquid water is only present in the cathode
- High enough electrical conductivity of the electrode to neglect electrical resistance
- Negligible contact resistance between the flow-fields and MEA
- Knudsen effects were not taken into account to simplify the model, as in [54, 55]

Isothermal operation is a reasonable assumption for fuel cell simulation on a local scale where numerous studies report a maximum temperature difference of less than 3 K within an MEA [56-58]. This assumption is especially well-suited to our fractal flow-field model, due to the symmetry associated with the fractal design.

Table 2. Parameters used in the model.

Geometry	Value	Units	Source	Parameter	Value	Units	Source
A	10^{-3}	m^2		t_{GDL}	350×10^{-6}	m	[59]
r_{agg}	150×10^{-9}	m	[35]	t_{CL}	40×10^{-6}	m	[60]
$W_{c,1}$	0.25×10^{-2}	m		t_{mem}	150×10^{-6}	m	[61]
Operating conditions							
P	1.1	atm	[62]	x_{O2}	0.11	-	[35]
T	353	K	[63]	x_{N2}	0.42	-	[35]
$S_{Cathode}$	2.0	-	[64]	x_w	0.47	-	[35]
S_{Anode}	2.0	-	[65]	U_{ref}	1.0	V	[53]

Physical properties							
$C_{O2,ref}$	0.85	mol m^{-3}	[63]	$i_{0,c,273}$	1.0×10^{-2}	A m^{-2}	[53]
$C_{H2,ref}$	56.4	mol m^{-3}	[66]	$i_{0,c}$	$i_{0,c,273} \times 2^{(T-273)/10}$	A m^{-2}	[67]
α_c	1.0	-	[64]	$i_{0,a}$	1.0×10^{2}	A m^{-2}	[40]
α_a	0.5	-	[52]	μ_w	3.5×10^{-4}	kg m^{-1} s^{-1}	[68]
H_{H2}	4.5×10^{-2}	atm m^3 mol^{-1}	[66]	ρ_C	2.0×10^{3}	kg m^{-3}	[63]
H_{O2}	3.56×10^{-1}	atm m^3 mol^{-1}	[69]	ρ_{Pt}	2.15×10^{4}	kg m^{-3}	[63]
n	$0.11 \times \lambda$	-	[70]	$\varepsilon_{V,GDL}$	0.75	-	[71]
λ	$C_{W,N}/C_f$	-	[53]	$\varepsilon_{V,CL}$	0.5	-	[35]
$C_{W,N}$	4.2×10^{3}	mol m^{-3}	[53]	$\varepsilon_{agg,N}$	0.66	-	[35]
C_f	1.2×10^{3}	mol m^{-3}	[53]	m_{pt}	4.0×10^{-3}	kg m^{-2}	[35]
k_v	100	atm^{-1} s^{-1}	[53]	k_c	100	s^{-1}	[53]
$Pt\|C$	0.28	-	[35]				
Transport properties							
$K_{w,0\text{-}GDL}$	2.0×10^{-15}	m^2	[53]	$D_{O2,H2O}$	$2.82 \times 10^{-5} \times (T/308.1)^{1.5}$	m^2 s^{-1}	[72]
$K_{w,0\text{-}CL}$	5.0×10^{-17}	m^2	[53]	$D_{O2,N2}$	$2.2 \times 10^{-5} \times (T/293.2)^{1.5}$	m^2 s^{-1}	[72]
σ_m	8.9	S m^{-1}	[35]	$D_{N2,H2O}$	$2.56 \times 10^{-5} \times (T/307.5)^{1.5}$	m^2 s^{-1}	[72]
σ_s	1000	S m^{-1}	[73]	$D_{H2,H2O}$	$9.15 \times 10^{-5} \times (T/307.5)^{1.5}$	m^2 s^{-1}	[72]
$D_{O2,w}$	4.73×10^{-9}	m^2 s^{-1}	[35]	$D_{O2,N}$	8.45×10^{-10}	m^2 s^{-1}	[63]

2.3. Incorporation of fractal flow-field design into the model

The fractal flow-fields comprise self-similar, repeatedly branching "H" shaped channels designed to uniformly distribute reactants across the catalyst layer surface [20, 21] (Fig. 3). This channel geometry allows a single inlet to branch into 4^N outlets *via* flow paths that are all equal in length. The fractal similarity dimension, D, is calculated by [74]:

$$D = \frac{\log(n)}{\log\left(\frac{1}{s}\right)} = \frac{\log(4)}{\log(2)} = 2 \quad (1)$$

where n is the number of daughter shapes per parent, and s is the contraction ratio between daughter and parent. The fractal dimension, D, is a measure for the space-filling capacity of an object; for self-similar objects, in which parts of the object are invariant under magnification, as in this recursively constructed tree, D is calculated by the above expression [74]. Contrary to classical objects from Euclidean geometry, the dimension of a fractal object is greater than its topological dimension [75], which would be 1 for a line, and can take non-integer values. The highest possible value of D is the dimension of the embedding space, which 2 for a plane, so, generally, $1 \leq D \leq 2$. The more the tree tends to occupy the plane, the higher the value of D

[76]. In our case, $D = 2$ indicates that, for an infinite number of generations, the branching tree would become plane-filling. Reactant depletion over the channel path is eliminated with this fractal structure, as only the outlets of the fractal distributor are open to the active area.

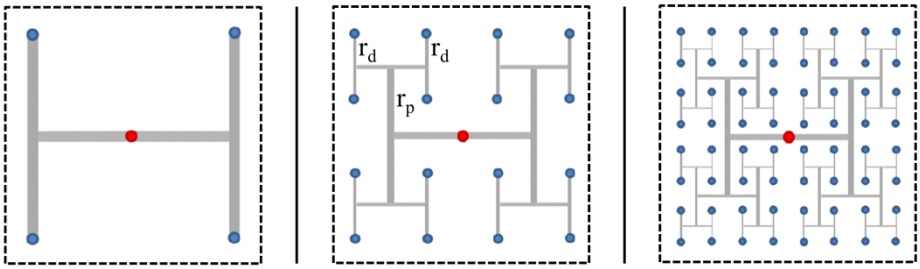

Fig. 3. Fractal structures of different generations N for gas distribution networks in PEMFCs. Red and blue dots represent fluid inlet and outlets, respectively, and dashed boxes represent active membrane area. Each H shape represents 4 daughter branches of radius r_d; the radius of each branch in an H shape is the same, including the horizontal channel.

Similar to the lung, the width of the channels in the fractal flow-fields was scaled by adopting Murray's law, which dictates a cubic relationship between hydraulic diameters of parent and daughter branches, leading to minimum mechanical energy and thermodynamic losses [74, 77-80]:

$$r_p^3 = \sum_{i=1}^{n} r_{d_i}^3 \tag{2}$$

Here, r_p (m) and r_d (m) are the radii of the parent and n daughter branches, respectively (here, $n = 4$). By following Murray's law, the scaling of the channel diameters leads to a reduction in flow velocity at each generation, due to a net increase in cross-sectional area. Similar scaling of the channel lengths leads to a constant pressure drop over each generation of the branching network, which minimizes the pressure drop required to drive the flow across the system [78]. This resembles the transition in flow regimes between bronchial tree (convection) and alveoli (diffusion) in the human lung, where gas transport has been shown to be optimal based on irreversible thermodynamics [78].

The ratio of convective and diffusive fluxes in the last generation of the fractal flow-field is characterized by the dimensionless Péclet number, defined as:

$$Pé = \frac{L \cdot U}{\mathcal{D}} \tag{3}$$

where L (m) is the GDL thickness, U (m s^{-1}) is the average gas velocity within the GDL, and $\mathcal{D}$ (m^2 s^{-1}) is the diffusivity. The flow velocity at the flow-field | GDL interface is calculated using:

$$U = \frac{Q_0}{A_N \cdot 4^N} \tag{4}$$

where Q_0 (m^3 s^{-1}) is the volumetric flow rate of gas at the inlet, and A_N (m^2) is the cross-sectional area of a single fractal outlet at the N^{th} generation. Eq. (4) determines the gas flow velocity at the GDL | flow-field inlet boundary. The velocity calculated using this equation is valid for all individual fractal outlets, since the distance between the fractal inlet and individual outlet channels is exactly the same, thus, allowing for equal distribution of inlet gas and equal velocity through individual outlet channels. The optimal number of fractal generations, N, in the flow-field is such that transport transitions from convective to diffusive, corresponding to a local Pé ~ 1. For Pé numbers less than 1 (Pé < 1), transport resistance in the finer channels would increase unnecessarily.

2.4. Governing equations for saturated agglomerate model

A steady-state, two-phase, two-dimensional saturated agglomerate model has been employed to model transport and reaction in the catalyst layer [53], while a modified reaction term [35], detailed in the further described Eq. (21), is incorporated to account for the spherical geometry of the catalyst agglomerates (Fig. 4).

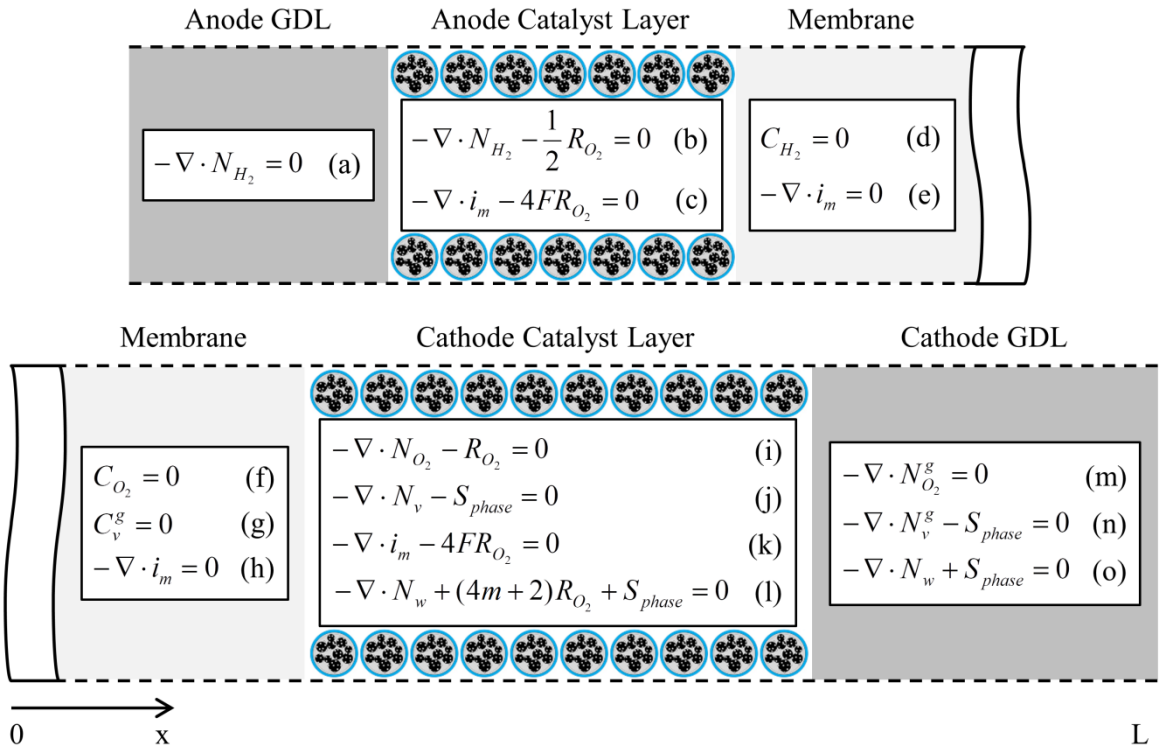

Fig. 4. Summary of governing equations in each domain of the PEMFC. All the terms are presented in detail in the following sections. Domains are not drawn to scale.

2.4.1. Transport of gas species within the GDL and CL

The continuity equation (Eq. 5) and Darcy's law (Eq. 6) are used to evaluate the velocity and pressure profiles of the gaseous mixture inside the porous media:

$$\nabla.\left(\rho_g \cdot u_g\right) = 0 \tag{5}$$

$$u_g = \frac{-k_p}{\mu_g} \cdot \nabla P \tag{6}$$

where ρ_g (kg m^{-3}), u_g (m s^{-1}), and μ_g (Pa s) are the density, velocity, and viscosity of the gaseous mixture, respectively, k_p (m^2) is the permeability of the porous medium, and P (Pa) is the pressure. The Stefan-Maxwell equations are used to describe the multi-component diffusion:

$$\nabla x_i = \sum_{j=1, j\neq i} \frac{1}{C \cdot D_{ij}^{eff}} \cdot \left(x_i \cdot N_j - x_j \cdot N_i\right) \tag{7}$$

where D_{ij}^{eff} (m^2 s^{-1}) is the effective binary diffusivity of species i in species j, x_i is the mole fraction of species i, N_i (mol m^{-2} s^{-1}) is the molar flux of species i, and C (mol m^{-3}) is the total molar concentration of gas. The transport of each gaseous species is governed by a general convection-diffusion equation in conjunction with the Stefan-Maxwell equations to account for multispecies diffusion:

$$\nabla \cdot \left\{ \frac{-\rho_g \cdot w_i \cdot \sum_j D_{ij}^{eff} \left[\nabla x_j + \left(x_j - w_j \right) \cdot \nabla P \right]}{P} \right\} = M_i \cdot S_i - \rho \cdot u_g \cdot \nabla w_i \quad (8)$$

where w_i and S_i (kg m^{-3} s^{-1}) are the mass fraction and source term of species i, respectively. The Bruggeman correlation is used to calculate the effective gas diffusion coefficient [53, 81-86], which accounts for the reduction in pore space available due to the presence of liquid water within the porous media:

$$D_{ij}^{eff} = D_{ij} \cdot \left[\varepsilon^v \cdot \left(1 - s \right) \right]^{1.5} \quad (9)$$

where ε^v, s, and D_{ij} (m^2 s^{-1}) are the void fraction of the porous medium, saturation, and binary diffusivity, respectively.

2.4.2. Transport of liquid water through the GDL and CL

Liquid water transport inside the GDL and catalyst layer is driven by capillary force and, hence, Darcy's law is used to describe the flow of liquid inside the porous medium [53]:

$$N_w = -\frac{\rho_w}{M_w} \cdot \left[\frac{K_w(s)}{\mu_w} \cdot \nabla P_l \right] \quad (10)$$

where P_l (Pa), ρ_W (kg m^{-3}), K_W (m^2), M_W (kg mol^{-1}), and μ_W (Pa s) are the pressure, density, permeability, molecular weight, and viscosity of liquid water, respectively. Analytical equations (Eqs. 11-14) for the description of capillary pressure (P_c), permeability of the porous medium (K_W), and capillary diffusion coefficient (D_c) are listed below.

The capillary pressure is expressed by the following empirical correlation [87]:

$$P_c(s) = P_g - P_l = d \cdot \left[e^{-a_1(s-c)} - e^{-a_2(s-c)} \right] + b \quad (11)$$

where s is the saturation level, P_g (Pa) is the gas phase pressure, and a_1, a_2, b, c, and d are fitting parameters (Table 3). The parameters used for the GDL have been obtained for carbon paper type [53].

Table 3. Parameters for the capillary pressure correlation in the GDL and CL [53].

Capillary function	a_1	a_2	b (Pa)	c	d (Pa)
GDL	-17.3	-25.1	32.3	0.350	-4.06
Catalyst layer	-23.5	-17.4	477	0.460	-3.58

The permeability of the porous medium depends on the liquid water saturation [87] as given by Eq. (12):

$$K_w(s) = K_{w,0} \cdot s^{4.5} \quad (12)$$

where $K_{w,0}$ (m^2) is the permeability of liquid water at 100% saturation level [88]. Substituting Eqs. (11) and (12) into Eq. (10) yields the following expression for the liquid water flux:

$$N_w = -\frac{\rho_w \cdot K_{w,0}}{M_w \cdot \mu_w} \cdot s^{4.5} \cdot \nabla P_c = -D_c \cdot \frac{\rho_w}{M_w} \cdot \nabla s \quad (13)$$

where the capillary diffusion coefficient, D_c ($m^2\ s^{-1}$), is defined as [53]:

$$D_c = -\frac{K_{w,0}}{\mu_w} \cdot \frac{dP_c}{ds} \cdot s^{4.5} \quad (14)$$

Saturation is assumed to be continuous within the GDL and the CL. However, saturation is not continuous at the GDL | CL interface, due to different pore sizes. This discontinuity is accounted for by assuming equal capillary pressure at the GDL | CL interface, which results in a saturation jump at the interface [53].

2.4.3. Transport of dissolved water through the polymer electrolyte membrane

The transport of dissolved water in the membrane is driven by electro-osmotic drag, diffusion due to the concentration gradient, and hydraulic permeation. However, since the model assumes fuel cell operation at constant pressure, the hydraulic permeation term is neglected. Hence, the water flux in the membrane can be simplified to:

$$N_w^N = \frac{i_N \cdot m}{F} - D_w^N \cdot \nabla C_w^N \tag{15}$$

where i_N (A m^{-2}) is the electrolyte current density vector, m is the electro-osmotic drag coefficient, D_W^N (m^2 s^{-1}) and C_W^N (mol m^{-3}) are the diffusivity and concentration of water in membrane, respectively. At steady state, the flux of water is constant, so that, using Eq. (15):

$$\nabla.\left(\frac{i_N \cdot m}{F}\right) = 0 \tag{16}$$

2.4.4. Transport of charge

The governing equations for the electronic and ionic charge transport are described using Ohm's law as:

$$i_s = -\sigma_s \cdot \nabla \phi_s \tag{17}$$

$$i_N = -\sigma_N \cdot \nabla \phi_N \tag{18}$$

where σ_s and σ_N (S m^{-1}) are the electronic and ionic conductivities, and ϕ_s and ϕ_N (V) are the solid and electrolyte phase potentials, respectively. The charge balance equations (Eqs. 17 and 18) are solved to obtain solid and electrolyte phase potentials:

$$\nabla.\left(-\sigma_N \cdot \nabla \phi_N\right) = S_\phi \tag{19}$$

$$\nabla.\left(-\sigma_s \cdot \nabla \phi_s\right) = -S_\phi \tag{20}$$

In the catalyst layer, the source term S_ϕ represents the rate of reaction, $4FR_{O2}$ (A m^{-3}). S_ϕ is zero in the polymer electrolyte membrane and GDL, as no reaction takes place in these domains.

2.4.5. Local rate of reaction in the catalyst layer

Assuming that the catalyst layer comprises a continuum of individual spherical catalyst agglomerates, the oxygen reduction reaction rate (mol m^{-3} s^{-1}) can be described by [35]:

$$R_{O_2} = \left[\frac{\frac{R \cdot T}{H_{O_2}}}{\frac{\delta_N \cdot (\delta_N + r_{agg})}{r_{agg} \cdot a_r \cdot D_{O_2}^N} + \frac{\delta_w \cdot (\delta_w + \delta_N + r_{agg})}{(\delta_N + r_{agg}) \cdot a_r \cdot D_{O_2}^w} + \frac{1}{\xi \cdot k_t}} \right] \cdot C_{O_2} \quad (21)$$

where R (8.314 J mol^{-1} K^{-1}) is the universal gas constant, H_{O2} (atm m^3 mol^{-1}) is Henry's constant of oxygen between air and electrolyte [89-93], δ_N and δ_w (m) are the ionomer and water film thicknesses surrounding an agglomerate, r_{agg} (m) is the agglomerate radius, $D_{O_2}^N$ and $D_{O_2}^w$ (m^2 s^{-1}) are the diffusivity of oxygen in ionomer and water, a_r (m^2 m^{-3}) is the effective agglomerate surface area, ξ is the agglomerate effectiveness factor, and k_t (s^{-1}) is the reaction rate constant. The first and second term in the denominator describe the diffusion of oxygen through the water and ionomer film, while the final term accounts for diffusion and reaction inside the agglomerate. The reaction rate constant k_t is expressed by:

$$k_t = \left(1 - \varepsilon_v^{CL}\right) \cdot \frac{a_{Pt}^{agg} \cdot i_{0,c}}{4 \cdot F \cdot C_{O_2}^{ref}} \cdot \exp\left[\frac{-\alpha_c \cdot F}{R \cdot T} \cdot \left(V_A - \phi_m - U_{eq}\right) \right] \quad (22)$$

where ε_v^{CL} is the catalyst layer porosity, $i_{0,c}$ (A m^{-2}) is the reference exchange current density for the cathode, $C_{O_2}^{ref}$ (mol m^{-3}) is the reference oxygen concentration in the catalyst layer, α_c is the cathodic transfer coefficient, V_A (V) is the applied cell voltage, U_{eq} (V) is the standard equilibrium potential of the oxygen reduction reaction, and ϕ_m (V) is the membrane potential. The effect of the catalyst morphology is taken into account by the active catalyst surface area per unit volume of agglomerates, a_{Pt}^{agg} (m^2 m^{-3}), which is defined as:

$$a_{Pt}^{agg} = \frac{a_{Pt} \cdot m_{Pt}}{t_{CL} \cdot \left(1 - \varepsilon_v^{CL}\right)} \tag{23}$$

where m_{Pt} (g_{Pt} m^{-2}) is the platinum loading, t_{CL} (m) is the catalyst layer thickness, and a_{Pt} (m^2 g^{-1}) is the surface area per unit mass of platinum particle, which is estimated from the empirical correlation for platinum supported catalyst [63]:

$$\alpha_{Pt} = 227.79 \cdot (Pt|C)^3 - 158.57 \cdot (Pt|C)^2 - 201.53 \cdot (Pt|C) + 159.5 \tag{24}$$

where $Pt|C$ is the platinum to carbon ratio in a catalyst agglomerate. The calculated value of a_{Pt} is 95.6 m^2 g^{-1}.

The relation between $Pt|C$, m_{pt}, and t_{CL} is given by [35]:

$$\varepsilon_s^{cl} = \left(\frac{1}{\rho_{Pt}} + \frac{1 - Pt|C}{\rho_{Pt} \cdot Pt|C} \right) \frac{m_{Pt}}{t_{cl}} \tag{25}$$

The effectiveness factor, ξ, for a spherical agglomerate in Eq. (21) is given by:

$$\xi = \frac{1}{\varphi} \cdot \frac{3 \cdot \varphi \cdot \coth(3 \cdot \varphi) - 1}{3 \cdot \varphi} \tag{26}$$

where the Thiele modulus, φ, is equal to [35]:

$$\varphi = \frac{r_{agg}}{3} \cdot \sqrt{\frac{k_t}{\left(1 - \varepsilon_v^{CL}\right) \cdot D_{O_2,eff}^N}} \tag{27}$$

The use of the Thiele modulus for the calculation of the effectiveness factor of spherical agglomerates is based on the assumption that the interior pore space of agglomerates is void of liquid water. Although this does not fully reflect the actual condition within the catalyst agglomerates, the use of the Thiele modulus for PEMFC simulations is still common practice, with models showing remarkable agreement with experimental data [39, 51, 94]. Accounting for the presence of liquid water in the interior pore space would lead to some quantitative changes in the results, *i.e.,* a reduction in the predicted overall cell performance. However, the general trend in performance improvement with respect to branching generations should

remain unchanged. This is because the improvement in fuel cell performance stems primarily from better distribution of reactant gas across the catalyst layer, instead of within the catalyst agglomerates. The effective oxygen diffusivity inside the agglomerates can also be expressed as a function of the pore volume fraction (ε_N^{agg}) and the tortuosity (τ_{agg}) via eqn. (28) [95]:

$$D_{O_2,eff}^N = D_{O_2}^N \cdot \frac{\varepsilon_N^{agg}}{\tau_{agg}} \tag{28}$$

The water film thickness is related to the liquid saturation level in the catalyst layer and it can be estimated by [35, 53]:

$$\delta_w = \frac{\varepsilon_v^{CL} \cdot s}{a_r} \tag{29}$$

The effective agglomerate surface area, a_r (m^2 m^{-3}), is defined as the outer surface area of the agglomerates per unit volume of the catalyst layer, and is given by:

$$a_r = \frac{3}{r_{agg} \cdot \left(1-\varepsilon_v^{CL}\right)} \tag{30}$$

where r_{agg} (m) is the catalyst agglomerate radius. The effectiveness factor of the hydrogen oxidation reaction (HOR) is set to 1.0, because hydrogen dissolves rapidly into the electrolyte, and the Butler-Volmer equation is used to describe the HOR kinetics [96]:

$$R_{H_2} = a_{Pt}^{agg} \cdot i_{0,a} \cdot \left(\frac{P_{H_2}}{C_{H_2}^{ref} \cdot H_{H_2}} \right)^{0.5} \cdot \left[\exp\left(\frac{-\left(1-\alpha_a\right) \cdot F \cdot \eta_a}{R \cdot T} \right) - \exp\left(\frac{\alpha_a \cdot F \cdot \eta_a}{R \cdot T} \right) \right] \tag{31}$$

where $i_{0,a}$ (A m^{-2}) is the reference exchange current density for the anode, P_{H2} (Pa) is the partial pressure of hydrogen, $C_{H_2}^{ref}$ (mol m^{-3}) is the reference hydrogen concentration in the catalyst layer, H_{H2} (atm m^3 mol^{-1}) is Henry's constant of hydrogen between air and electrolyte, α_a is the anodic transfer coefficient, and η_a is the anodic overpotential.

2.4.6. Water phase change

The rate of water phase change (mol m^{-3} s^{-1}) in the porous medium is expressed by [53]:

$$S_{phase}=\begin{cases} k_c \cdot \dfrac{\varepsilon_i^v \cdot (1-s)\cdot y_v}{R\cdot T}\cdot\left(y_v \cdot P - P_v^{sat}\right) & y_v \cdot P \geq P_v^{sat} \\ k_v \cdot \dfrac{\varepsilon_i^v \cdot s \cdot \rho_w}{M_w}\cdot\left(y_v \cdot P - P_v^{sat}\right) & y_v \cdot P < P_v^{sat} \end{cases} \quad (32)$$

where y_v is the mole fraction of liquid water, ρ_w (kg m^{-3}) is the density of liquid water, M_w (kg mol^{-1}) is the molar weight of water, P (Pa) is the total pressure, k_c and k_v (s^{-1}) are the condensation and evaporation rate constant, respectively. The vapor saturation pressure, P_v^{sat} (Pa), is calculated using the Antoine equation [97]:

$$P_v^{sat} = \exp\left[16.3872 - \frac{3885.7}{(T-273.15)+230.17}\right] \quad (33)$$

Boundary conditions used in this model are outlined in supplementary information.

3. Simulation procedure

3.1. Inlet fractal flow-field

The domain described in Fig. 2 was modeled using the finite element solver COMSOL v.5. Simulations were conducted using a DELL Precision T3500 workstation with 24 GB of RAM and a 3.2 GHz Intel Xeon processor; each simulation lasted approximately 60 seconds. The gas diffusion and catalyst layers were described by the parameters listed in Table 2. A series of parametric sweeps over the number of branching generations and GDL thickness was used to determine the effect of the fractal flow-field architecture on the overall fuel cell performance. The stoichiometry ratio of 2, a common value invoked in commercial fuel cell systems, was used for both cathode and anode, and the simulation was performed at an operating voltage of 0.4 V throughout, unless otherwise stated. Such operating conditions were chosen to represent

a regime of operation expected to be limited by reactant access to the electrode, so that the advantages of the fractal flow-field could be expected to become important.

The main solution variables we are solving for in this simulation include gas velocity (u_g), gas pressure (P), capillary pressure (P_c), mole (x_i) and mass (w_i) fraction of individual gas species, saturation (s), solid (ϕ_s), and electrolyte (ϕ_N) phase potentials, rate of water phase change (S_{phase}), and reaction rate constant (k_t).

3.2. Optimization of the microstructure

Parameters optimized with respect to power density (P_D) and platinum utilization (U_{Pt}) were obtained using objective functions proposed in previous studies [35, 98]. The objective function for P_D optimization aims to maximize the current density within the cathode catalyst layer, and is defined as follows [98]:

$$4FV \cdot \max\left[\int_{(L-t_{CL})}^{L} R_{O_2}\, dx\right] \tag{34}$$

with: $0.12 < \varepsilon_s^{CL} < 1;\ 0.12 < \varepsilon_N^{CL} < 1; 0.25 < \varepsilon_v^{CL} < 1; 0.01 < m_{Pt} < 1.0;$ and $0.10 < Pt|C < 0.90$.

The objective function for U_{Pt} optimization seeks to achieve high power density at low platinum loading, and is expressed as follows [35]:

$$4FV \cdot \max\left[\frac{\int_{(L-t_{CL})}^{L} R_{O_2}\, dx}{m_{Pt}}\right] \tag{35}$$

with the same constraints, as well as: $P_D > 0.20 \frac{W}{cm^2}$.

The constraints on volume fractions ensure proper percolation in each phase (solid, ionomer, gas). The constraint on minimum power density ensures that the microstructure can generate

sufficient power density, while keeping the platinum loading low. Parameters not listed under Eqs. (34) and (35), such as r_{agg}, δ_{agg}, δ_{GDL}, and ε_v^{GDL}, were kept constant during optimization.

4. Simulation results and discussion

4.1. Effect of the number of branching generations on fuel cell performance

Increasing the number of branching generations, N, has two effects on the resultant concentration distribution in the porous medium. Firstly, with each additional generation, the distance between adjacent gas outlets is reduced, leading to an increasingly uniform boundary condition along the flow-field | GDL interface. Secondly, each subsequent generation increases the total cross-sectional area of the outlets of the fractal inlet channels, thereby lowering the velocity of the reactant gas and, ultimately, allowing the convective flux at a channel outlet to approach the diffusive flux in the GDL.

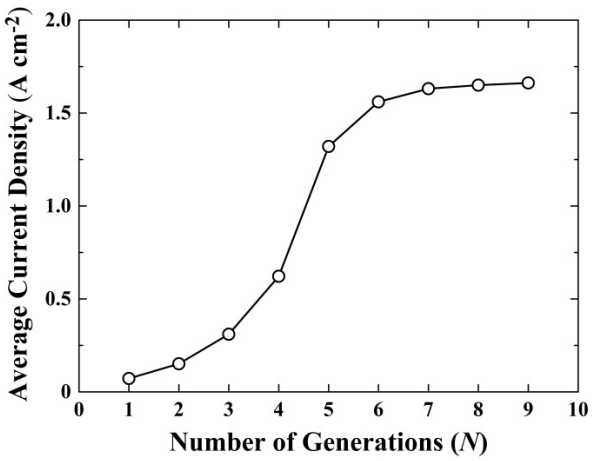

Fig. 5. Change in average current density with respect to the number of generations, N. Simulation results were obtained for 100% RH.

Fig. 5 illustrates the performance of the lung-inspired flow-field based PEMFC as a function of the number of generations (stoichiometry ratio of 2 in anode and cathode, 0.4 V operating voltage, see section 3.1). At low generation levels (N = 1 to 4), the spacing between adjacent distributor inlets is large (>> GDL thickness) and the flow exiting the final generation is

convection dominated (Pé > 1; Table 4). Therefore, only sub-sections of the active area directly in the projection of the inlet are exposed to an appreciable amount of oxygen for reaction [20]. This leads to a highly non-uniform gas distribution across the plane of the catalyst layer and low fuel cell performance.

A sharp increase in fuel cell performance occurs between $N = 3$ and $N = 6$ generations, as the convective flux becomes equal to the diffusion flux at the exits for $N \sim 6$ (Pé ~ 1; Table 4), and the spacing between inlets is sufficiently small to engender more uniform concentration profiles at the GDL | CL interface.

At higher generations ($N \geq 8$), the spacing between adjacent inlets becomes very small (< 100 μm) and diffusion takes over as the dominant transport mechanism in the final generation and GDL (Pé < 1; Table 4). The resultant concentration profile at the catalyst layer interface is essentially completely uniform. As a result, a plateau in fuel cell performance is observed and additional generations (higher N) provide little benefit. Table 4 summarizes key geometric parameters for the simulation conducted in this study.

To validate the model, the theoretical results were compared to experimental results obtained at 100% RH for $N = 3$ and 4, and 50% RH for $N = 5$. The current densities obtained at 0.4 V for $N = 3$, 4, and 5 were 0.64, 0.76, and 1.10 A cm^{-2}, which correspond to a deviation of ~ 52%, 19%, and 20%, respectively [20]. The discrepancy between experimental and simulation results for $N = 3$ may have arisen from the 2D approximation, assuming uniform removal of unreacted reactant and product *via* fractal outlet channels. Despite this approximation, the deviation for $N = 4$ and 5 from the theoretical results is small, which indicates that the simplified model provides accurate results in these situations, where more uniformity is envisioned. Hence, this simplified model can be used for the optimization of the thickness of the GDL and the cathode catalyst layer (CCL) microstructure.

Table 4

Summary of fractal flow-field simulations with standard composition cathode catalyst layer.

N	Number of outlets	Outlet spacing (μm)	Outlet width (μm)	Pé
3	64	4000	992	3.89
4	256	1800	625	2.45
5	1024	823	394	1.54
6	4096	378	248	0.97
7	16384	170	156	0.61
8	65536	74.7	98.0	0.39
9	262144	30.9	62.0	0.24

4.2. Effect of the number of branching generations on GDL thickness.

The incorporation of a fractal flow-field to homogenize reactant concentration at the catalyst layer | GDL interface makes the GDL partially redundant, since they serve the same purpose. Therefore, the GDL does not need to be as thick to provide the same degree of homogenization. By reducing its thickness, additional concentration losses (resulting from the concentration gradient across the GDL) can be avoided. As a result, utilizing a thinner GDL would provide a higher concentration of reactant gas to the catalyst layer, further enhancing fuel cell performance.

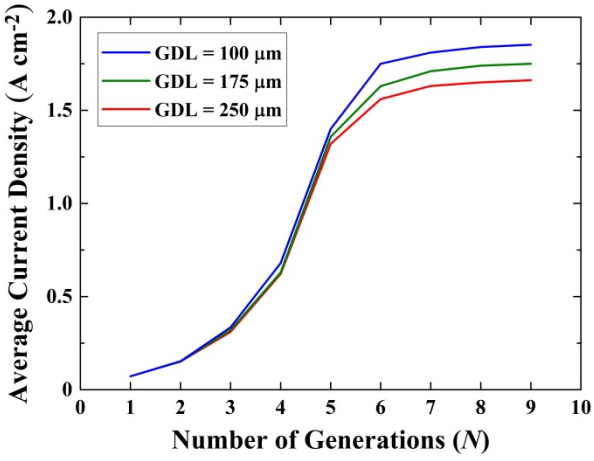

Fig. 6. Effect of GDL thickness on fuel cell performance. Simulation results were obtained for 100% RH.

A similar trend in fuel cell performance is observed up to $N = 5$ generations for different GDL thicknesses (Fig. 6). At these low generations, a decrease in GDL thickness merely exacerbates

the variation in current density across the GDL | CL interface and does not enhance the fuel cell performance. The increased local current density in the region adjacent to the inlet is offset by a sharp decline in local current density under the land and outlet channels, due to diminished transverse reactant transport in thinner GDLs [99-101] (Fig. 7 (a)).

At higher generations ($N \geq 5$), an improvement in fuel cell performance is observed, as reactant mass transport is facilitated by increasing the reactant concentration gradient across the catalyst layer. This result is consistent with previous reports in the literature demonstrating an increase in fuel cell performance *via* the utilization of thinner GDLs [32, 99, 102, 103], due to enhanced mass transport. It is important to note that transport in the GDL is not limiting for N < 5, but GDL thickness plays a role between N = 5 and 6, as the effective reaction rate within the catalyst layer has then sufficiently increased such that the GDL plays a role in adding transport resistance, if it is too thick.

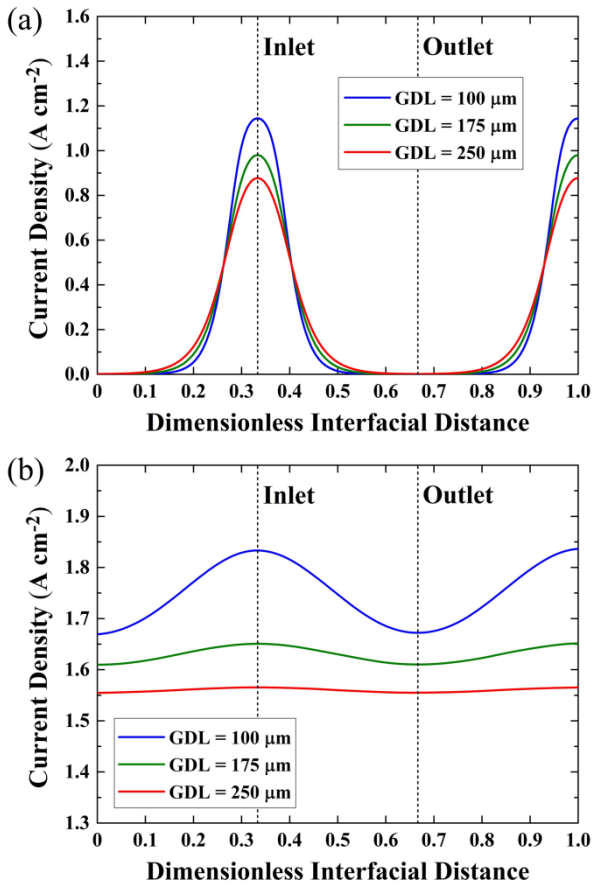

Fig. 7. Effect of gas diffusion layer thickness on local cell current density for (a) $N = 3$ and (b) $N = 6$ (inlet positions at $x \sim 0.33$ and 1; outlet positions at $x \sim 0$ and 0.67). Simulation results were obtained for 100% RH. This Figure was rotated clockwise by 90° for ease of visualization.

Additionally, thinner GDLs enhance local current density as a direct consequence of higher oxygen concentration across the catalyst layer (Fig. 7 (b)). This observation is in slight contrast with previous reports exhibiting a small drop in current density under the land and outlet channels with thinner GDLs as a result of reduced lateral mass transport [99-101]. However, the reported aggravated reactant depletion near the outlet channels with thinner GDLs is circumvented for higher generation ($N \geq 5$) fractal flow-fields due to their shorter path length between inlet and outlet channels, which subjects the entire catalyst layer to higher reactant concentration and current density. The reduction in lateral mass transport with thinner GDLs is not completely attenuated, though, as suggested by the suppressed improvement in current density in areas adjacent to the outlet channels, compared to the inlet channels (Fig. 7 (b)). Besides the improved fuel cell performance using a thinner GDL, an additional benefit of up to ~ 25% reduction in cell thickness and volumetric power density of the stack is realized, given a commercial cell thickness of 1.2 mm.

Table 5

Results of microstructure optimization to maximize power density (P_D) and platinum utilization (U_{Pt}) in the cathode catalyst layer.

Cathode catalyst	m_{Pt} (mg_{Pt} cm^{-2})	$Pt\|C$	ε_v^{CL}	ε_s^{CL}	ε_N^{CL}	$\varepsilon_{N,agg}$	t_{CL} (μm)
Base design	0.40	0.28	0.50	0.13	0.37	0.66	40
P_D optimized	0.18	0.29	0.25	0.13	0.62	0.78	18
U_{Pt} optimized	0.01	0.27	0.25	0.14	0.61	0.77	1.0

4.3. Fractal flow-field with optimized cathode catalyst layers

Apart from the thickness of the GDL, the cathode catalyst layer (CCL) also plays a pivotal role in determining the performance of PEMFCs. From the perspective of fuel cell performance and cost, generating sufficient power density, while lowering the catalyst loading and improving

catalyst utilization, are key criteria to design an efficient catalyst layer. Here, fractal flow-fields are coupled with the CCL microstructures, which were independently optimized with respect to maximum platinum utilization (U_{Pt}) and power density (P_D) under the assumption of uniform reactant concentration profile across the flow-field | GDL interface, as proposed by Marquis and Coppens [35, 98] (Table 5) and presented in section 3.2. While the ionomer fraction in the P_D and U_{Pt} optimized CCL are higher than values typically reported in the literature, the higher Nafion content is accounted for by a much thinner catalyst layer. Also, in the case of a U_{Pt} optimized CCL, the lower reaction rate (due to ultra-low platinum loading) diminishes the effect of diffusion limitations and, therefore, allows for a higher ionomer fraction in the catalyst layer. The radius of the catalyst agglomerates is known to significantly dictate the performance of the CCL. While not included as a design variable in this work, a value of 100 nm is chosen to minimise any diffusion limitations occurring within the agglomerates themselves [35].

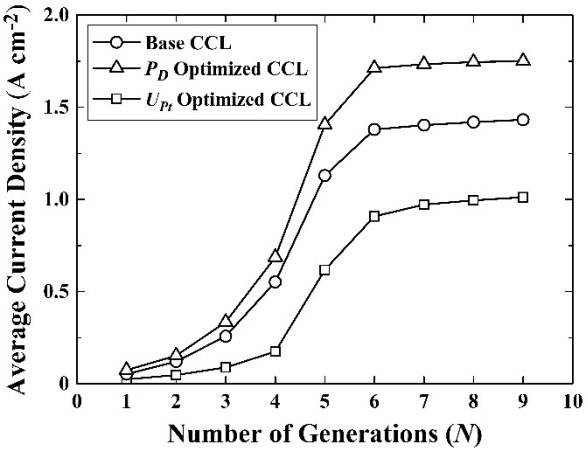

Fig. 8. Simulation results showing the effect of the number of fractal branching generations on average cell current density for the base and optimized CCL (cathode catalyst layer) microstructures. The operating conditions are $S_{Anode} = 1.5$, $S_{Cathode} = 2$, $r_{agg} = 100$ nm, and 100% RH.

Fig. 8 compares the fractal flow-field performance of U_{Pt} and P_D optimized CCL microstructures to the base design at different generations N. The trend in fuel cell performance improvement is similar to previous results, differing only in the magnitude of change in the average current density.

The P_D optimized CCL microstructure displays the highest average current density at $N \geq 5$, despite its lower platinum loading than the base (non-optimized microstructure) CCL (Table 5). Its optimized microstructure alleviates the diffusion limitations inside the catalyst layer and agglomerates, resulting in a ~ 20% increase in average current density (Fig. 8). With less branching generations ($N < 5$), the P_D optimized CCL microstructure performance improvement over the base microstructure is lower, indicating that non-uniform gas distribution limits mass transport towards the catalyst layer and, hereby, catalyst utilization. A significant portion of the catalyst layer adjacent to the outlet channels is oxygen-depleted, and, thus, the optimized catalyst layer in these regions does not result in higher current density.

On the contrary, the U_{Pt} optimized CCL exhibits the lowest average current density due to its low platinum loading (~ 40 times lower than the base design) resulting in a low reaction rate [35]. Despite its low intrinsic performance, the U_{Pt} optimized CCL as a whole surpasses the DoE target for platinum utilization of ~ 8 kW/g_{Pt} [104] at $N = 4$ generations, and plateaus at approximately 36 kW/g_{Pt} at $N = 6$ generations (Fig. 9). This finding suggests that either the platinum loading or the number of cells in the stack could potentially be reduced by ~ 75%, allowing for a significant cost reduction in the electrocatalyst and fuel cell components. The ultra-low platinum loading of a U_{Pt} optimized CCL allows exposure of appreciable oxygen concentration to platinum catalyst along the radius of the agglomerates, enhancing platinum utilization. Its significantly thinner catalyst layer (Table 5) also facilitates gas diffusion and proton conduction across the CCL, improving mass transport across the CCL and subsequent platinum utilization.

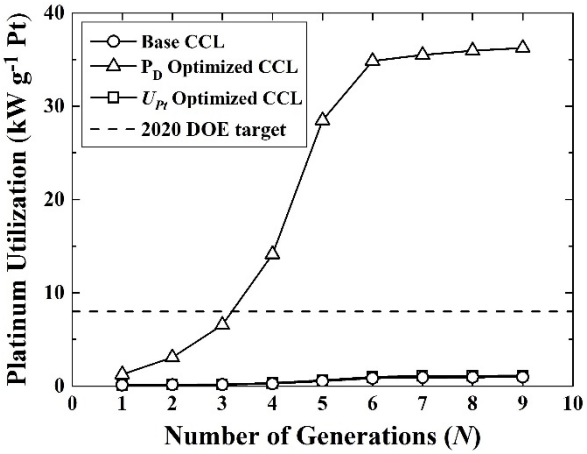

Fig. 9. Simulation results showing the effect of the number of fractal branching generations on platinum utilization for the base and optimized CCL microstructures. The operating conditions are $S_{Anode} = 1.5$, $S_{Cathode} = 2$, $r_{agg} = 100$ nm, and 100% RH.

The base and P_D optimized cathode CL designs demonstrate substandard platinum utilization for all generations, since metal nanoparticles situated towards the center of an agglomerate are subjected to extremely low oxygen concentrations, due to significant diffusion limitations arising from surplus catalyst loading. A small improvement in platinum utilization with respect to the number of generations indicates that platinum utilization is not limited by reactant distribution across the electrode, but by reactant transport within the catalyst agglomerate. Collectively, these results show that proper design of catalyst layer microstructure and platinum loading, factors that predominantly determine oxygen concentration profile within an agglomerate, is indispensable to realize enhanced platinum utilization from a uniform gas distribution.

5. Conclusions

A finite-element model of a lung-inspired flow-field based PEMFC was presented. This model was used to determine the effect of the number of branching generations, *N*, on the required thickness of the GDL and fuel cell performance.

Introduction of a fractal flow-field to homogenize reactant concentration at the flow-field | GDL interface allows for a thinner GDL to be used. Fuel cell performance is enhanced further with a thinner GDL, as a result of higher oxygen concentration across the catalyst layer for a higher number of branching generations, N. However, the reduction in lateral mass transport with thinner GDLs only leads to minimal improvement in fuel cell performance for lower numbers of generations ($N \leq 5$).

The finite-element model of the lung-inspired flow-field based PEMFC was coupled with cathode catalyst layer (CCL) microstructures optimized with respect to platinum utilization (U_{Pt}) and power density (P_D). Despite its lower platinum loading, the P_D optimized CCL yields a higher average current density than the base design, because of a microstructure that facilitates diffusion within the catalyst layer. In the case of a U_{Pt} optimized CCL, the ultra-low platinum loading significantly lowers the reaction rate, resulting in a reduced fuel cell current density.

In terms of platinum utilization, the U_{Pt} optimized CCL surpasses the 2020 DoE target for platinum utilization of ~ 8 kW/g_{Pt} for $N = 4$ generations, and achieves a value of ~ 36 kW/g_{Pt} when $N = 6$. The base and P_D optimized microstructures demonstrate extremely low platinum utilization, due to substantial oxygen deprivation towards the center of the catalyst agglomerates from surplus platinum loading. A multi-objective optimization involving platinum loading and power density may be beneficial to evaluate the trade-off between the objectives for the design of efficient and robust fuel cell catalyst layers.

An important aspect of PEMFC operation using a fractal flow-field is how liquid water is handled in the gas channels. Water transport across a channel cannot be investigated on a 2D domain; a 3D model should be developed to substantiate the effect of channel geometries on water removal, despite the high computational cost. Fortunately, however, this may not be necessary: By integrating the capillary-based water management strategy recently developed

538 in our group[105, 106] with the fractal flow-fields, flooding in the cathode should be pre-
539 empted, which would lead to robust and reliable fuel cell performance, irrespective of the
540 operating conditions. Therefore, the advantages of a uniform gas flow could be preserved also
541 at higher branching ratios, *N*.
542 To further improve the model presented in this manuscript, the following aspects have to be
543 implemented: *i*) percolation theory instead of the Bruggeman equation to account for reduced
544 connectivity of the pores by using an adaptation of recent pore network modeling approaches
545 developed by our group in collaboration with ECUST.[107, 108] The percolation theory
546 ensures that the effective diffusivity is zero below the percolation threshold, when a connected
547 gas diffusion network ceases to exist. [53, 109]; *ii*) temperature effects to monitor the changes
548 in liquid water content in the fuel cell under different experimental conditions [110-113]; and
549 *iii*) local resistance in the form of an oxygen transport barrier to capture transport losses at the
550 surface of the catalyst layer microstructure [114-118].
551

552 **Declaration of interest**

553 Declarations of interest: none
554

555 **Acknowledgement**

556 The authors wish to thank the US National Science Foundation Fuel Cell IGERT at Rensselaer
557 (grant number DGE-0504361) for supporting the start of this work. Continued research at UCL
558 was made possible thanks to financial support from an EPSRC “Frontier Engineering” Award
559 (grant number EP/K038656/1) and a UCL Faculty of Engineering Sciences Dean’s Scholarship.
560
561
562

563 **Nomenclature**

A	active area, m^2
A_N	cross-sectional area of a single outlet at the N^{th} generation, m^2
a_r	effective agglomerate surface area, $m^2\ m^{-3}$
a_{Pt}	effective catalyst surface area, $m^2\ g^{-1}$
C	total gas concentration, $mol\ m^{-3}$
C_f	fixed charge site concentration in membrane, $mol\ m^{-3}$
C_{H2}^{ref}	reference concentration of hydrogen, $mol\ m^{-3}$
C_{O2}	concentration of oxygen in catalyst layer, $mol\ m^{-3}$
C_{O2}^{ref}	reference concentration of oxygen, $mol\ m^{-3}$
C_{O2}^{air}	concentration of oxygen in inlet air, $mol\ m^{-3}$
C_v^g	concentration of vapor, $mol\ m^{-3}$
$C_v^{g,air}$	concentration of water vapor in inlet air, $mol\ m^{-3}$
C_w^N	water concentration in membrane, $mol\ m^{-3}$
D	fractal dimension
$\mathcal{D}$	diffusivity ($m^2\ s^{-1}$)
D_c	capillary diffusion coefficient, $m^2\ s^{-1}$
D_{ij}	element of the Maxwell-Stefan diffusion coefficient matrix, $m^2\ s^{-1}$
D_{O2}^N	oxygen diffusivity in Nafion, $m^2\ s^{-1}$
$D_{O2,N}^{eff}$	effective oxygen diffusivity in Nafion, $m^2\ s^{-1}$
D_{O2}^w	oxygen diffusivity in water, $m^2\ s^{-1}$
D_w^N	diffusivity of water in Nafion, $m^2\ s^{-1}$
F	Faraday's constant, $96500\ C\ mol^{-1}$

H	Henry's constant, atm m^3 mol^{-1}
i_N	electrolyte current density, A m^{-2}
i_d	current density, A m^{-2}
i_s	electronic current density, A m^{-2}
i_0	exchange current density, A m^{-2}
k_c	condensation rate constant, s^{-1}
k_p	electrode permeability, m^2
k_v	evaporation rate constant, atm^{-1} s^{-1}
k_t	reaction rate constant, s^{-1}
K_w	water permeability, m^2
$K_{w,0}$	water permeability at 100% saturation, m^2
L	width of fractal outlet at the final generation, m
m_{pt}	platinum loading per unit area of catalyst layer, g_{Pt} m^{-2}
M_i	molecular weight, kg mol^{-1}
m	electro-osmotic drag coefficient
N	number of fractal generations
N_i^g	flux of gaseous species i, mol m^{-2} s^{-1}
N_v^g	flux of vapor, mol m^{-2} s^{-1}
N_w	flux of liquid water, mol m^{-2} s^{-1}
N_w^g	flux of water vapor, mol m^{-2} s^{-1}
N_w^N	flux of liquid water in membrane, mol m^{-2} s^{-1}
P	total pressure, Pa
P_c	capillary pressure, Pa
P_D	power density, W cm^{-2}

P_g	gas pressure, Pa
P_i	partial pressure, Pa
P_l	liquid pressure, Pa
P^{sat}	saturation pressure, Pa
U_{Pt}	platinum utilization, kW g^{-1}_{Pt}
$Pt\|C$	mass percentage of platinum catalyst on carbon black, kg Pt / (kg C + kg Pt)
Q_o	volumetric flow rate of gas at the inlet, m^3 s^{-1}
r_{agg}	agglomerate radius, m
R	ideal gas constant, 8.314 J mol^{-1} K^{-1}
R_i	reaction rate, mol m^{-3} s^{-1}
S_{Anode}	anode stoichiometry ratio, 2
$S_{Cathode}$	cathode stoichiometry ratio, 2
S_{phase}	evaporation/condensation rate, mol m^{-3} s^{-1}
s	liquid water saturation
S	source term
T	temperature, K
t_{CL}	catalyst layer thickness, m
t_{GDL}	gas diffusion layer thickness, m
t_{mem}	membrane thickness, m
u_g	gas phase velocity, m s^{-1}
U_{eq}	standard equilibrium potential, V
V	voltage, V
V_A	operating voltage, V
$W_{c,1}$	initial channel width, m

w_i mass fraction of species *i*

x_i mole fraction of species *i*

y_v mole fraction of liquid water

Greek

α charge transfer coefficient

a_{Pt}^{agg} specific catalyst surface area, $m^2\ m^{-3}$

δ_N Nafion film thickness, m

δ_W water film thickness, m

ε_N^{agg} agglomerate-ionomer volume fraction, m^3 ionomer m^{-3} agglomerate

ε^v void phase volume fraction

η overpotential, V

μ viscosity, Pa s

ξ effectiveness factor

ρ density, kg m^{-3}

σ_m ionic conductivity, S m^{-1}

σ_s electronic conductivity, S m^{-1}

τ tortuosity

ϕ potential, V

φ Thiele modulus

ϕ_N membrane phase potential, V

Superscripts and subscripts

0 intrinsic

a anode

agg	agglomerate
c	cathode
CL	catalyst layer
eff	effective
eq	equilibrium
g	gas
GDL	gas diffusion layer
H_2	hydrogen
i	species *i*
j	species *j*
mem	membrane
N	Nafion
N_2	nitrogen
O_2	oxygen
Pt	platinum
ref	reference
s	solid phase
v	void phase / vapor
w	liquid water

564

565

566

567

568

569

References

1. Pollet, B.G., S.S. Kocha, and I. Staffell, *Current status of automotive fuel cells for sustainable transport.* Current Opinion in Electrochemistry, 2019. **16**: p. 90-95.
2. Arvay, A., et al., *Nature inspired flow field designs for proton exchange membrane fuel cell.* International Journal of Hydrogen Energy, 2013. **38**(9): p. 3717-3726.
3. Wu, H.-W., *A review of recent development: Transport and performance modeling of PEM fuel cells.* Applied Energy, 2016. **165**: p. 81-106.
4. Wang, C., et al., *The respective effect of under-rib convection and pressure drop of flow fields on the performance of PEM fuel cells.* 2017. **7**: p. 43447.
5. Wu, Y., et al., *Effect of serpentine flow-field design on the water management of polymer electrolyte fuel cells: An in-operando neutron radiography study.* Journal of Power Sources, 2018. **399**: p. 254-263.
6. Trogadas, P., T.F. Fuller, and P. Strasser, *Carbon as catalyst and support for electrochemical energy conversion.* Carbon, 2014. **75**: p. 5-42.
7. Taniguchi, A., et al., *Analysis of electrocatalyst degradation in PEMFC caused by cell reversal during fuel starvation.* Journal of Power Sources, 2004. **130**(1): p. 42-49.
8. Schmittinger, W. and A. Vahidi, *A review of the main parameters influencing long-term performance and durability of PEM fuel cells.* Journal of Power Sources, 2008. **180**(1): p. 1-14.
9. Narimani, M., J. DeVaal, and F. Golnaraghi, *Hydrogen emission characterization for proton exchange membrane fuel cell during oxygen starvation – Part 1: Low oxygen concentration.* International Journal of Hydrogen Energy, 2016. **41**(8): p. 4843-4853.
10. Trogadas, P., et al., *Hierarchically Structured Nanomaterials for Electrochemical Energy Conversion.* Angewandte Chemie International Edition, 2016. **55**(1): p. 122-148.
11. Trogadas, P., J. Parrondo, and V. Ramani, *Degradation Mitigation in Polymer Electrolyte Membranes Using Cerium Oxide as a Regenerative Free-Radical Scavenger.* Electrochemical and Solid-State Letters, 2008. **11**(7): p. B113-B116.
12. Trogadas, P., J. Parrondo, and V. Ramani, *CeO2 Surface Oxygen Vacancy Concentration Governs in Situ Free Radical Scavenging Efficacy in Polymer Electrolytes.* ACS Applied Materials & Interfaces, 2012. **4**(10): p. 5098-5102.
13. Kulkarni, N., et al., *Effect of cell compression on the water dynamics of a polymer electrolyte fuel cell using in-plane and through-plane in-operando neutron radiography.* Journal of Power Sources, 2019. **439**: p. 227074.
14. Wawdee, P., et al., *Water transport in a PEM fuel cell with slanted channel flow field plates.* International Journal of Hydrogen Energy, 2015. **40**(9): p. 3739-3748.
15. Kozakai, M., et al., *Improving gas diffusivity with bi-porous flow-field in polymer electrolyte membrane fuel cells.* International Journal of Hydrogen Energy, 2016. **41**(30): p. 13180-13189.
16. Guo, N., M.C. Leu, and U.O. Koylu, *Network based optimization model for pin-type flow field of polymer electrolyte membrane fuel cell.* International Journal of Hydrogen Energy, 2013. **38**(16): p. 6750-6761.
17. Guo, N., M.C. Leu, and U.O. Koylu, *Bio-inspired flow field designs for polymer electrolyte membrane fuel cells.* International Journal of Hydrogen Energy, 2014. **39**(36): p. 21185-21195.
18. Hamilton, P.J. and B.G. Pollet, *Polymer Electrolyte Membrane Fuel Cell (PEMFC) Flow Field Plate: Design, Materials and Characterisation.* Fuel Cells, 2010. **10**(4): p. 489-509.
19. Whiteley, M., et al., *A novel polymer electrolyte fuel cell flow-field: The through-plane array.* Journal of Power Sources, 2019. **442**: p. 227218.
20. Trogadas, P., et al., *A lung-inspired approach to scalable and robust fuel cell design.* Energy & Environmental Science, 2018. **11**(1): p. 136-143.

21. Kjelstrup, S., et al., *Nature-inspired energy-and material-efficient design of a polymer electrolyte membrane fuel cell.* Energy & Fuels, 2010. **24**(9): p. 5097-5108.
22. Coppens, M.-O., *A nature-inspired approach to reactor and catalysis engineering.* Current Opinion in Chemical Engineering, 2012. **1**(3): p. 281-289.
23. Ozden, A., et al., *Designing, modeling and performance investigation of bio-inspired flow field based DMFCs.* International Journal of Hydrogen Energy, 2017. **42**(33): p. 21546-21558.
24. Vyatskikh, A., et al., *Additive manufacturing of 3D nano-architected metals.* Nature Communications, 2018. **9**(1): p. 593.
25. Luca, H., et al., *Additive Manufacturing of Metal Structures at the Micrometer Scale.* Advanced Materials, 2017. **29**(17): p. 1604211.
26. Bourell, D.L., *Perspectives on Additive Manufacturing.* Annual Review of Materials Research, 2016. **46**(1): p. 1-18.
27. Adilet, Z., et al., *Additive Manufacturing: Unlocking the Evolution of Energy Materials.* Advanced Science, 2017. **4**(10): p. 1700187.
28. Ligon, S.C., et al., *Polymers for 3D Printing and Customized Additive Manufacturing.* Chemical Reviews, 2017. **117**(15): p. 10212-10290.
29. Limjeerajarus, N. and P. Charoen-amornkitt, *Effect of different flow field designs and number of channels on performance of a small PEFC.* International Journal of Hydrogen Energy, 2015. **40**(22): p. 7144-7158.
30. Lim, B.H., et al., *Effects of flow field design on water management and reactant distribution in PEMFC: a review.* Ionics, 2016. **22**(3): p. 301-316.
31. Wang, C., et al., *Effect of height/width-tapered flow fields on the cell performance of polymer electrolyte membrane fuel cells.* International Journal of Hydrogen Energy, 2017. **42**(36): p. 23107-23117.
32. Cindrella, L., et al., *Gas diffusion layer for proton exchange membrane fuel cells—A review.* Journal of Power Sources, 2009. **194**(1): p. 146-160.
33. Park, S., J.-W. Lee, and B.N. Popov, *A review of gas diffusion layer in PEM fuel cells: Materials and designs.* International Journal of Hydrogen Energy, 2012. **37**(7): p. 5850-5865.
34. Lee, J., et al., *Investigating the effects of gas diffusion layer substrate thickness on polymer electrolyte membrane fuel cell performance via synchrotron X-ray radiography.* Electrochimica Acta, 2017. **236**: p. 161-170.
35. Marquis, J. and M.-O. Coppens, *Achieving ultra-high platinum utilization via optimization of PEM fuel cell cathode catalyst layer microstructure.* Chemical Engineering Science, 2013. **102**: p. 151-162.
36. Berning, T. and N. Djilali, *Three-dimensional computational analysis of transport phenomena in a PEM fuel cell—a parametric study.* Journal of Power Sources, 2003. **124**(2): p. 440-452.
37. Lum, K.W. and J.J. McGuirk, *Three-dimensional model of a complete polymer electrolyte membrane fuel cell – model formulation, validation and parametric studies.* Journal of Power Sources, 2005. **143**(1): p. 103-124.
38. Du, C.Y., et al., *Parametric study of a novel cathode catalyst layer in proton exchange membrane fuel cells.* Journal of Power Sources, 2006. **160**(1): p. 224-231.
39. Khajeh-Hosseini-Dalasm, N., et al., *A parametric study of cathode catalyst layer structural parameters on the performance of a PEM fuel cell.* International Journal of Hydrogen Energy, 2010. **35**(6): p. 2417-2427.
40. Marr, C. and X. Li, *Composition and performance modelling of catalyst layer in a proton exchange membrane fuel cell.* Journal of Power Sources, 1999. **77**(1): p. 17-27.
41. Tiedemann, W. and J. Newman, *Maximum Effective Capacity in an Ohmically Limited Porous Electrode.* Journal of The Electrochemical Society, 1975. **122**(11): p. 1482-1485.

42. You, L. and H. Liu, *A parametric study of the cathode catalyst layer of PEM fuel cells using a pseudo-homogeneous model.* International Journal of Hydrogen Energy, 2001. **26**(9): p. 991-999.
43. Dobson, P., et al., *Characterization of the PEM Fuel Cell Catalyst Layer Microstructure by Nonlinear Least-Squares Parameter Estimation.* Journal of The Electrochemical Society, 2012. **159**(5): p. B514-B523.
44. Ebrahimi, S., R. Roshandel, and K. Vijayaraghavan, *Power density optimization of PEMFC cathode with non-uniform catalyst layer by Simplex method and numerical simulation.* International Journal of Hydrogen Energy, 2016. **41**(47): p. 22260-22273.
45. Ridge, S.J., et al., *Oxygen Reduction in a Proton Exchange Membrane Test Cell.* Journal of The Electrochemical Society, 1989. **136**(7): p. 1902-1909.
46. Shah, A.A., et al., *Transient non-isothermal model of a polymer electrolyte fuel cell.* Journal of Power Sources, 2007. **163**(2): p. 793-806.
47. Wang, G., P.P. Mukherjee, and C.-Y. Wang, *Optimization of polymer electrolyte fuel cell cathode catalyst layers via direct numerical simulation modeling.* Electrochimica Acta, 2007. **52**(22): p. 6367-6377.
48. Xing, L., et al., *Multi-variable optimisation of PEMFC cathodes based on surrogate modelling.* International Journal of Hydrogen Energy, 2013. **38**(33): p. 14295-14313.
49. Hu, G., et al., *Optimization and parametric analysis of PEMFC based on an agglomerate model for catalyst layer.* Journal of the Energy Institute, 2014. **87**(2): p. 163-174.
50. Xing, L., et al., *Numerical investigation of the optimal Nafion® ionomer content in cathode catalyst layer: An agglomerate two-phase flow modelling.* International Journal of Hydrogen Energy, 2014. **39**(17): p. 9087-9104.
51. Moein-Jahromi, M. and M.J. Kermani, *Performance prediction of PEM fuel cell cathode catalyst layer using agglomerate model.* International Journal of Hydrogen Energy, 2012. **37**(23): p. 17954-17966.
52. Sun, W., B.A. Peppley, and K. Karan, *An improved two-dimensional agglomerate cathode model to study the influence of catalyst layer structural parameters.* Electrochimica acta, 2005. **50**(16): p. 3359-3374.
53. Wang, X. and T.V. Nguyen, *Modeling the Effects of Capillary Property of Porous Media on the Performance of the Cathode of a PEMFC.* Journal of The Electrochemical Society, 2008. **155**(11): p. B1085-B1092.
54. Molaeimanesh, G.R., M.A. Bamdezh, and M. Nazemian, *Impact of catalyst layer morphology on the performance of PEM fuel cell cathode via lattice Boltzmann simulation.* International Journal of Hydrogen Energy, 2018. **43**(45): p. 20959-20975.
55. Zhan, N., W. Wu, and S. Wang, *Pore network modeling of liquid water and oxygen transport through the porosity-graded bilayer gas diffusion layer of polymer electrolyte membrane fuel cells.* Electrochimica Acta, 2019. **306**: p. 264-276.
56. Zamel, N. and X. Li, *Non-isothermal multi-phase modeling of PEM fuel cell cathode.* International Journal of Energy Research, 2010. **34**(7): p. 568-584.
57. Cao, T.-F., et al., *Modeling the temperature distribution and performance of a PEM fuel cell with thermal contact resistance.* International Journal of Heat and Mass Transfer, 2015. **87**: p. 544-556.
58. Hashemi, F., S. Rowshanzamir, and M. Rezakazemi, *CFD simulation of PEM fuel cell performance: Effect of straight and serpentine flow fields.* Mathematical and Computer Modelling, 2012. **55**(3): p. 1540-1557.
59. Mortazavi, M. and K. Tajiri. *Impact of Gas Diffusion Layer Properties on Liquid Water Breakthrough Pressure in Polymer Electrolyte Fuel Cell*. in *ASME 2013 11th International Conference on Fuel Cell Science, Engineering and Technology collocated with the ASME 2013 Heat Transfer Summer Conference and the ASME 2013 7th International Conference on Energy Sustainability*. 2013. American Society of Mechanical Engineers.

60. Weber, A.Z. and J. Newman, *Effects of membrane-and catalyst-layer-thickness nonuniformities in polymer-electrolyte fuel cells.* Journal of the Electrochemical Society, 2007. **154**(4): p. B405-B412.
61. Mittal, V.O., H.R. Kunz, and J.M. Fenton, *Membrane degradation mechanisms in PEMFCs.* Journal of The Electrochemical Society, 2007. **154**(7): p. B652-B656.
62. Zhou, B., et al., *Water and pressure effects on a single PEM fuel cell.* Journal of Power Sources, 2006. **155**(2): p. 190-202.
63. Secanell, M., et al., *Multi-variable optimization of PEMFC cathodes using an agglomerate model.* Electrochimica Acta, 2007. **52**(22): p. 6318-6337.
64. Weber, A.Z., R.M. Darling, and J. Newman, *Modeling two-phase behavior in PEFCs.* Journal of the Electrochemical Society, 2004. **151**(10): p. A1715-A1727.
65. Qu, S., et al., *The effect of air stoichiometry change on the dynamic behavior of a proton exchange membrane fuel cell.* Journal of Power Sources, 2008. **185**(1): p. 302-310.
66. Bernardi, D.M. and M.W. Verbrugge, *A mathematical model of the solid-polymer-electrolyte fuel cell.* Journal of the Electrochemical Society, 1992. **139**(9): p. 2477-2491.
67. Pasaogullari, U. and C.-Y. Wang, *Two-phase modeling and flooding prediction of polymer electrolyte fuel cells.* Journal of The Electrochemical Society, 2005. **152**(2): p. A380-A390.
68. Wang, Y. and X. Feng, *Analysis of reaction rates in the cathode electrode of polymer electrolyte fuel cell I. Single-layer electrodes.* Journal of The Electrochemical Society, 2008. **155**(12): p. B1289-B1295.
69. Sander, R., *Compilation of Henry's law constants for inorganic and organic species of potential importance in environmental chemistry*. 1999, Max-Planck Institute of Chemistry, Air Chemistry Department Mainz, Germany.
70. Springer, T.E., T.A. Zawodzinski, and S. Gottesfeld, *Polymer Electrolyte Fuel Cell Model.* Journal of The Electrochemical Society, 1991. **138**(8): p. 2334-2342.
71. Berning, T., M. Odgaard, and S.K. Kær, *Water balance simulations of a polymer-electrolyte membrane fuel cell using a two-fluid model.* Journal of Power Sources, 2011. **196**(15): p. 6305-6317.
72. Cussler, E.L., *Diffusion: Mass Transfer in Fluid Systems*. 3rd ed. 2009: Cambridge University Press.
73. Bevers, D., et al., *Simulation of a polymer electrolyte fuel cell electrode.* Journal of Applied Electrochemistry, 1997. **27**(11): p. 1254-1264.
74. Mandelbrot, B.B., *The Fractal Geometry of Nature*. 1983: W.H. Freeman, San Francisco.
75. Mandelbrot, B., *Fractals and Chaos: The Mandelbrot Set and Beyond*. 2004: Springer-Verlag, New York.
76. Vicsek, T., *Fractal Growth Phenomena*. 1989: World Scientific Publishing Company, Singapore.
77. Murray, C.D., *The physiological principle of minimum work: I. The vascular system and the cost of blood volume.* Proceedings of the National Academy of Sciences of the United States of America, 1926. **12**(3): p. 207.
78. Gheorghiu, S., et al., *Is the lung an optimal gas exchanger?*, in *Fractals in biology and medicine*. 2005, Springer. p. 31-42.
79. Mauroy, B., et al., *An optimal bronchial tree may be dangerous.* Nature, 2004. **427**: p. 633.
80. Sapoval, B., M. Filoche, and E.R. Weibel, *Smaller is better—but not too small: A physical scale for the design of the mammalian pulmonary acinus.* Proceedings of the National Academy of Sciences, 2002. **99**(16): p. 10411-10416.
81. Andersson, M., et al., *A review of cell-scale multiphase flow modeling, including water management, in polymer electrolyte fuel cells.* Applied Energy, 2016. **180**: p. 757-778.

82. Cetinbas, F.C., et al., *Microstructural Analysis and Transport Resistances of Low-Platinum-Loaded PEFC Electrodes.* Journal of The Electrochemical Society, 2017. **164**(14): p. F1596-F1607.
83. Gandomi, Y.A., et al., *Water Management in Polymer Electrolyte Fuel Cells through Asymmetric Thermal and Mass Transport Engineering of the Micro-Porous Layers.* Journal of The Electrochemical Society, 2016. **163**(8): p. F933-F944.
84. Myles, T.D., et al., *Application of an Effective Medium Formulation to Account for Transport Due to Fiber and Web-like Inclusions in Gas Diffusion Layers.* Journal of The Electrochemical Society, 2015. **162**(7): p. F645-F650.
85. Wang, Y. and S. Wang, *Evaluation and modeling of PEM fuel cells with the Bruggeman correlation under various tortuosity factors.* International Journal of Heat and Mass Transfer, 2017. **105**: p. 18-23.
86. Wong, K.H. and E. Kjeang, *Simulation of Performance Tradeoffs in Ceria Supported Polymer Electrolyte Fuel Cells.* Journal of The Electrochemical Society, 2019. **166**(2): p. F128-F136.
87. Ye, Q. and T. Van Nguyen, *Three-dimensional simulation of liquid water distribution in a PEMFC with experimentally measured capillary functions.* Journal of the Electrochemical Society, 2007. **154**(12): p. B1242-B1251.
88. Natarajan, D. and T. Van Nguyen, *Three-dimensional effects of liquid water flooding in the cathode of a PEM fuel cell.* Journal of Power Sources, 2003. **115**(1): p. 66-80.
89. Chen, L., Q. Kang, and W. Tao, *Pore-scale study of reactive transport processes in catalyst layer agglomerates of proton exchange membrane fuel cells.* Electrochimica Acta, 2019. **306**: p. 454-465.
90. Nalbant, Y., C.O. Colpan, and Y. Devrim, *Development of a one-dimensional and semi-empirical model for a high temperature proton exchange membrane fuel cell.* International Journal of Hydrogen Energy, 2018. **43**(11): p. 5939-5950.
91. Randrianarizafy, B., et al., *Design optimization of rib/channel patterns in a PEMFC through performance heterogeneities modelling.* International Journal of Hydrogen Energy, 2018. **43**(18): p. 8907-8926.
92. Rizvandi, O.B. and S. Yesilyurt, *A pseudo three-dimensional, two-phase, non-isothermal model of proton exchange membrane fuel cell.* Electrochimica Acta, 2019. **302**: p. 180-197.
93. Sohn, Y.-J., et al., *PEMFC modeling based on characterization of effective diffusivity in simulated cathode catalyst layer.* International Journal of Hydrogen Energy, 2017. **42**(18): p. 13226-13233.
94. Secanell, M., et al., *Optimization of a proton exchange membrane fuel cell membrane electrode assembly.* Structural and Multidisciplinary Optimization, 2009. **40**(1): p. 563.
95. Litster, S., et al., *Morphological Analyses of Polymer Electrolyte Fuel Cell Electrodes with Nano-Scale Computed Tomography Imaging.* Fuel Cells, 2013. **13**(5): p. 935-945.
96. Barbir, F., *PEM fuel cells: theory and practice*. 2nd ed. 2013, Amsterdam: Academic Press.
97. Smith, J.M., H.C. Van Ness, and M.M. Abbott, *Introduction to Chemical Engineering Thermodynamics*. 2005: McGraw-Hill.
98. Marquis, J., *Nature-inspired hierarchically structured high-efficiency PEM fuel cell*, in *Chemical & Biological Engineering*. , 2013, Rensselaer Polytechnic Institute: Troy, NY,. p. 202.
99. Jang, J.-H., W.-M. Yan, and C.-C. Shih, *Numerical study of reactant gas transport phenomena and cell performance of proton exchange membrane fuel cells.* Journal of Power Sources, 2006. **156**(2): p. 244-252.
100. Sun, W., B.A. Peppley, and K. Karan, *Modeling the Influence of GDL and flow-field plate parameters on the reaction distribution in the PEMFC cathode catalyst layer.* Journal of Power Sources, 2005. **144**(1): p. 42-53.

101. Chiang, M.-S. and H.-S. Chu, *Numerical investigation of transport component design effect on a proton exchange membrane fuel cell.* Journal of Power Sources, 2006. **160**(1): p. 340-352.
102. Jeng, K.T., et al., *Oxygen mass transfer in PEM fuel cell gas diffusion layers.* Journal of Power Sources, 2004. **138**(1): p. 41-50.
103. Jang, J.-H., W.-M. Yan, and C.-C. Shih, *Effects of the gas diffusion-layer parameters on cell performance of PEM fuel cells.* Journal of Power Sources, 2006. **161**(1): p. 323-332.
104. Guvelioglu, G.H. and H.G. Stenger, *Computational fluid dynamics modeling of polymer electrolyte membrane fuel cells.* Journal of Power Sources, 2005. **147**(1–2): p. 95-106.
105. Cho, J.I.S., et al., *Capillaries for water management in polymer electrolyte membrane fuel cells.* International Journal of Hydrogen Energy, 2018. **43**(48): p. 21949-21958.
106. Cho, J.I.S., et al., *Visualization of liquid water in a lung-inspired flow-field based polymer electrolyte membrane fuel cell via neutron radiography.* Energy, 2019. **170**: p. 14-21.
107. Ye, G., et al., *Method for generating pore networks in porous particles of arbitrary shape, and its application to catalytic hydrogenation of benzene.* Chemical Engineering Journal, 2017. **329**: p. 56-65.
108. Ye, G., et al., *Pore network modeling of catalyst deactivation by coking, from single site to particle, during propane dehydrogenation.* AIChE Journal, 2019. **65**(1): p. 140-150.
109. Eikerling, M. and A.A. Kornyshev, *Modelling the performance of the cathode catalyst layer of polymer electrolyte fuel cells.* Journal of Electroanalytical Chemistry, 1998. **453**(1): p. 89-106.
110. Owejan, J.P., et al., *Water Transport Mechanisms in PEMFC Gas Diffusion Layers.* Journal of The Electrochemical Society, 2010. **157**(10): p. B1456-B1464.
111. Thomas, A., et al., *Thermal and water transfer in PEMFCs: Investigating the role of the microporous layer.* International Journal of Hydrogen Energy, 2014. **39**(6): p. 2649-2658.
112. Weber, A.Z. and M.A. Hickner, *Modeling and high-resolution-imaging studies of water-content profiles in a polymer-electrolyte-fuel-cell membrane-electrode assembly.* Electrochimica Acta, 2008. **53**(26): p. 7668-7674.
113. Zhang, Z., W. Liu, and Y. Wang, *Three dimensional two-phase and non-isothermal numerical simulation of multi-channels PEMFC.* International Journal of Hydrogen Energy, 2019. **44**(1): p. 379-388.
114. Chen, L., et al., *Nanoscale simulation of local gas transport in catalyst layers of proton exchange membrane fuel cells.* Journal of Power Sources, 2018. **400**: p. 114-125.
115. Greszler, T.A., D. Caulk, and P. Sinha, *The Impact of Platinum Loading on Oxygen Transport Resistance.* Journal of The Electrochemical Society, 2012. **159**(12): p. F831-F840.
116. Jinnouchi, R., et al., *Molecular Dynamics Simulations on O2 Permeation through Nafion Ionomer on Platinum Surface.* Electrochimica Acta, 2016. **188**: p. 767-776.
117. Kurihara, Y., T. Mabuchi, and T. Tokumasu, *Molecular dynamics study of oxygen transport resistance through ionomer thin film on Pt surface.* Journal of Power Sources, 2019. **414**: p. 263-271.
118. Suzuki, T., K. Kudo, and Y. Morimoto, *Model for investigation of oxygen transport limitation in a polymer electrolyte fuel cell.* Journal of Power Sources, 2013. **222**: p. 379-389.